

Research Article

Terrain Matching Localization for Underwater Vehicle Based on Gradient Fitting

Jiaqi Gao , Dongdong Peng , Tian Zhou , Tianhao Wang , and Chao Xu 

Acoustic Science and Technology Laboratory, College of Underwater Acoustic Engineering, Harbin Engineering University, Harbin, China

Correspondence should be addressed to Tian Zhou; zhoutian@hrbeu.edu.cn

Received 26 June 2018; Accepted 22 October 2018; Published 30 December 2018

Academic Editor: Stelios M. Potirakis

Copyright © 2018 Jiaqi Gao et al. This is an open access article distributed under the Creative Commons Attribution License, which permits unrestricted use, distribution, and reproduction in any medium, provided the original work is properly cited.

Terrain matching positioning is a promising method to overcome the problem that the inertial navigation error of the underwater vehicle accumulates over time. In the conventional terrain matching method, all measurement points are commonly used for matching and positioning. However, this method fails to be taken into a balanced consideration on both the computation complexity and the positioning accuracy. To reduce the computation and ensure the accuracy at the same time, an improved terrain matching method based on the gradient fitting is proposed in this paper. In the method, the gradient distributions of multiple terrain regions are firstly analyzed. Then, normal distribution is used to fit them, and according to the distribution, points with larger gradient values are selected as matching points. Finally, minimum absolute difference matching is chosen to match for positioning. Simulation results using multibeam sonar show that the improved terrain matching localization method not only reduces the computational complexity but also improves the accuracy of positioning.

1. Introduction

Underwater vehicles are becoming more and more popular in marine fields. At present, most underwater navigation systems are inertial navigation systems (INS). As the error of INS inevitably accumulates over time [1], many auxiliary measures need to be adopted, including Global Positioning System- (GPS-) aided methods [2, 3], acoustic navigation methods [4, 5], and Doppler velocity log- (DVL-) aided methods [6, 7]. However, the limitation of these techniques is that the navigation system must rely on either electromagnetic wave signal (e.g., GPS signal), artificial beacons (e.g., long baseline), complex mathematical models (e.g., flow prediction model), or the accessibility of the sea bottom (e.g., DVL bottom tracking). It would be difficult to satisfy the demands of efficiency, mobility, and invisibility at the same time.

As an autonomous underwater vehicle (AUV) is generally equipped with pressure measurement sensor and multibeam sonar, topographic information becomes an available and reliable resource in aided navigation. The

terrain-aided navigation (TAN) system does not require any other external equipment, with high localization precision, favorable invisibility, complete autonomy, and no cumulative time error [8, 9]. TAN was first applied to cruise missiles and aircraft, such as the famous terrain contour matching (TERCOM) [10, 11] and Sandia inertial terrain-aided navigation (SITAN) systems [12]. In recent years, TAN's far-reaching application potential in marine fields has aroused widespread concern of many scholars. Algorithms for underwater topographic matching positioning and navigation have been proposed one after another, such as iterated closest contour point- (ICCP-) based [13], cross-correlation-based [14], and maximum likelihood estimation-based [15] terrain navigation. The ICCP-based terrain navigation algorithm works by single-beam sounding sonar, whereas the terrain navigation method which is based on correlation and maximum likelihood estimation is applicable to not only single-beam sonar but also multi-beam sonar. Compared with the single-beam sonar, multi-beam sonar can measure a survey line perpendicular to the track at a time, obtain more detailed topographical

information, and apply much more to terrain matching navigation [16].

The nonlinear Bayesian method is regarded as popular and state-of-the-art in TAN's algorithms. Literature [17, 18] demonstrates the ability of the TAN system using this method to sustain a high navigation accuracy, without the need of any external position measurements. The TAN system is built based on the motion of an AUV and the measurement of the bottom depth. Two common recursive Bayesian filter equations are used recursively to update the distribution of the position offsets for each time step, and the particle filter may be used as a sampled-based approximation to solve the optimal Bayesian filter equations. However, since each multibeam measurement is performed on hundreds of points and calculated thousands of times, the conventional matching algorithm that traverses all positions and calculates with all measured points is computationally expensive and un conducive to real-time positioning. Meanwhile, using uniform sampling points for matching may not guarantee the integrity of topographic information and it is inevitably affected by multibeam sonar measurement noise. In order to improve the performance of matching, terrain matching localization methods based on image processing are proposed in [19, 20]. However, the multibeam measurement noise may result in the distortion of natural terrain image, and it is uncertain which features of terrain would maximize the precise topographical information. Moreover, the feature extraction process is very time-consuming and greatly increases the extra computation.

To overcome the problem that the conventional terrain matching method fails to be taken into a balanced consideration in the computation complexity and the positioning accuracy, an effective sampling method of the matching points based on gradient distribution fitting is proposed in this paper, which is carried out from the strategy of selecting matching points. As the probability density function (PDF) of some common distributions (e.g., normal, gamma, and Weibull) is extensively used to characterize the normalized acquired data [21–23], the distribution which yields the lowest mean absolute error (MAE) would be chosen as the representation of the gradient data. The selection criteria of the matching points are proposed based on the quantile property of the fitting distribution, making the selection of the matching points more efficient and convenient. In this study, the fitting universality and computational efficiency of the normal distribution is proved, the criterion with optimum threshold is given, and according to the fitting distribution and best criterion, the measured depths with larger gradient values are selected as matching points for positioning. Different from the matching with uniform sampling points or all points, the matching based on gradient fitting can not only reduce the computation but also retain the main features of the terrain. Most importantly, the improved method reduces the influence of the adjacent or repetitive terrain and finally decreases the positioning error.

The rest of the paper is organized as follows. In Section 2, the conventional minimum absolute difference- (MAD-)

based TERCOM algorithm and the essence of its matching error are analyzed. Section 3 provides the comparison between three different distributions and gives the selection criteria. An improved algorithm is proposed under the criteria. Then, the simulation results are given in Section 4. The optimal threshold of the selection criteria is given, and the difference between the conventional algorithms and the improved algorithm in both error performance and computation is analyzed. Finally, some conclusions are given in Section 5.

2. Conventional TERCOM Algorithm

Most modern underwater terrain localization algorithms, based on mean absolute difference (MAD) or mean square difference (MSD), process the data from the multibeam sonar in batches to derive an accurate estimate of the AUV's position. This section will review the basic matching approach of the TERCOM method and analyze the essence of its limitation of localization performance.

2.1. Matching Approach. The depth values are measured as terrain data using multibeam sonar and then stored into batch files, called a measured profile, during a specific update period and are processed in batches using a correlation algorithm.

The digital elevation map (DEM) provided by bathymetric mapping sonar is a depth value function of discrete positions, represented by $z = z(x, y)$. Under a certain assumption of the map precision, the DEM can be converted into the $M \times N$ matrix with interpolation function H .

$$A(i, j) = H[z(x, y)], \quad 1 \leq i \leq M, 1 \leq j \leq N, \quad (1)$$

where M is the number of rows and N is the number of columns of matrix A .

In real-time navigation, the measured profile intervals provided by the multibeam sonar in the matching region are integrated and calculated. In the matching region, assume that position (x_0, y_0) is the center and terrain data $z' = z'(x, y)$ is the grouping of m consecutive profiles. The measured terrain elevation matrix can be written as

$$Z'_{x_0, y_0}(i, j) = H[z'(x, y)], \quad 1 \leq i \leq m, 1 \leq j \leq n, \quad (2)$$

where m and n are, respectively, determined by the numbers of profiles and beams ($m \ll M, n \ll N$). A reference matrix from the estimated position of the vehicle is determined in matrix A , as shown in Figure 1 and the following process.

Consider A 's top left $m \times n$ submatrix and its central (x_1, y_1)

$$Z_{x_1, y_1}(i, j) = A(i, j), \quad 1 \leq i \leq m, 1 \leq j \leq n. \quad (3)$$

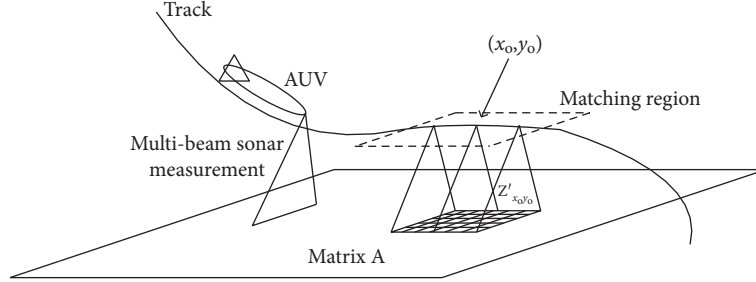


FIGURE 1: Schematic of TERCOM.

There is a relationship between the arbitrary position (x, y) and the proposed position (x_1, y_1)

$$\begin{cases} x = x_1 + sd' \\ y = y_1 + td' \end{cases}, \begin{cases} 0 \leq s \leq M - m, \\ 0 \leq t \leq N - n, \\ s, t \in N^*, \end{cases} \quad (4)$$

where d' is the matching interval. The reference matrix can be written as

$$\begin{aligned} Z_{xy}(i, j) &= Z_{x_1+sd_1, y_1+td_2}(i, j) = A\left(i + t \frac{d'}{d}, j + s \frac{d'}{d}\right) \\ &= A(i + tk, j + sk), \end{aligned} \quad (5)$$

where d is the width of the unit cell in the map and $d' = kd (k \in N^*)$.

Thus, the MAD used for correlating the measured terrain elevation matrix with each size corresponding reference matrix is defined as follow.

$$\begin{aligned} D_{xy} &= \frac{1}{mn} \sum_{i=1}^m \sum_{j=1}^n |Z_{xy}(i, j) - Z'_{x_0, y_0}(i, j)| \\ &= \frac{1}{mn} \sum_{i=1}^m \sum_{j=1}^n |A(i + tk, j + sk) - Z'_{x_0, y_0}(i, j)|. \end{aligned} \quad (6)$$

Finally, find index (s_0, t_0) of the minimum D_{xy}

$$D_{\min}(s_0, t_0) = \min_{\substack{0 \leq s \leq M-m, \\ 0 \leq t \leq N-n}} \{D_{xy}\} \quad (7)$$

and determine (\hat{x}_0, \hat{y}_0) as the position fix according to (4).

2.2. Applicability and Limitation. As the most widely known TAN algorithm, TERCOM is a correlation-oriented method using the collection of measured profiles rather than individual measurement recursive processing, which makes it insensitive to the initial position error and more stable to provide an accurate position fix to compensate for the navigation error of the INS. Meanwhile, the MAD correlation matching algorithm works as an efficient and robust way to determine the most relevant location in the DEM. With the

increasing measurement range and accuracy of multibeam sonar, the position estimation of the AUV becomes more reliable owing to a large number of accurate calculation points. Since the DEM provides underwater terrain depth values in a matrix form, the batch processing works on the assumption that the AUV moves along a rectilinear trajectory in the matching region. This MAD-based TERCOM algorithm is beneficial due to high accuracy and simplicity of usage compared to the recursive algorithms like SITAN.

However, a false position fix of the AUV resulting from the wrong MAD estimation may occur while moving over a flat terrain or repetitive terrain which has no terrain uniqueness. Although the expansion of the matching region leads to comparable localization performance, the bias caused by the attitude change of the AUV would inevitably be enlarged and so is the computation time. In order to obtain more suitable solutions for these limitations, the essence of the correlated estimation errors is expected to be revealed as follows.

Most of the bias in the measured terrain elevation matrix is caused by ambient noise, in addition to the sensor accuracy, interpolation function, tidal fluctuations, and other factors. The measured terrain elevation matrix can be represented by

$$\begin{aligned} Z'_{x_0, y_0}(i, j) &= Z_{x_0, y_0}(i, j) + N(i, j), \\ 1 \leq i \leq m, 1 \leq j \leq n, \end{aligned} \quad (8)$$

where $N(i, j)$ is the bias at point (i, j) . According to (6), the MAD at position (x_0, y_0) can be written as

$$D_{x_0, y_0} = \frac{1}{mn} \sum_{i=1}^m \sum_{j=1}^n |N(i, j)|. \quad (9)$$

Moreover, the relationship of the reference matrixes between position (x_0, y_0) and adjacent position $(x_0 + \alpha, y_0 + \beta)$ can be depicted as

$$\lim_{\alpha \rightarrow 0, \beta \rightarrow 0} Z_{x_0 + \alpha, y_0 + \beta}(i, j) = Z_{x_0, y_0}(i, j). \quad (10)$$

In the flat terrain or repetitive terrain, even if α and β are considerably large, there is still

$$Z_{x_0 + \alpha, y_0 + \beta}(i, j) \approx Z_{x_0, y_0}(i, j), \quad (11)$$

and with the influence of $N(i, j)$, the value of the difference $D_{x_0y_0}$ is not small enough to be distinguished from $D_{x_0+\alpha, y_0+\beta}$, which ultimately leads to a false position fix.

3. Improved Algorithm

In the following sections, we formulate a solution both for the improvement of localization accuracy and for the reduction of computing time utilizing calculating point selection based on depth gradient fitting. The formulation and process of the improved algorithm are described in Section 3.1 and 3.2, respectively. Section 3.3 lists the preconditions of the proposed algorithm. Section 3.4 realizes the depth gradient fitting and puts forward a feasible distribution, and Section 3.5 provides selection criteria of matching points based on the property of the proposed distribution.

3.1. Formulation. Consider the real-time position (x_0, y_0) and its adjacent positions $(x_0 \pm d', y_0)$ and $(x_0, y_0 \pm d')$. Due to the large overlap of the depth matrices in the adjacent positions, the reference matrixes are related in most of i and j , which can be depicted by

$$\begin{aligned} Z_{x_0 \pm d', y_0}(i, j) &= Z_{x_0 y_0}(i, j \pm k), \\ Z_{x_0, y_0 \pm d'}(i, j) &= Z_{x_0 y_0}(i \pm k, j). \end{aligned} \quad (12)$$

According to (8), since $N(i, j)$ is relatively small compared to the depth, the absolute difference in the adjacent positions can be approximated as

$$\begin{aligned} D_1(i, j) &= \left| Z_{x_0 \pm d', y_0}(i, j) - Z'_{x_0 y_0}(i, j) \right| \\ &\approx \left| Z_{x_0 y_0}(i, j \pm k) - Z'_{x_0 y_0}(i, j) \right|, \\ D_2(i, j) &= \left| Z_{x_0, y_0 \pm d'}(i, j) - Z'_{x_0 y_0}(i, j) \right| \\ &\approx \left| Z_{x_0 y_0}(i \pm k, j) - Z'_{x_0 y_0}(i, j) \right|, \end{aligned} \quad (13)$$

where D_1 and D_2 represent the absolute difference of the positions adjacent to (x_0, y_0) in horizontal and vertical matching directions, respectively. Their average values determine the value of D_{xy} defined in (6) and ultimately influence the localization accuracy. Suppose if some specific (i, j) , which have relatively large values of D_1 or D_2 , can be efficiently sampled out and calculated, the position bias would be reduced together with the interference from the adjacent position.

3.2. Process Flow. Therefore, the following processes are constructed for the improved algorithm.

Step 1. Construct the gradient matrixes. The X -direction gradient matrix is defined as

$$\text{Grad}_x(i, j) = \begin{cases} \frac{Z'_{x_0 y_0}(i, 2) - Z'_{x_0 y_0}(i, 1)}{d}, & j = 1, \\ \frac{Z'_{x_0 y_0}(i, n) - Z'_{x_0 y_0}(i, n-1)}{d}, & j = n, \\ \frac{Z'_{x_0 y_0}(i, j+1) - Z'_{x_0 y_0}(i, j-1)}{2d}, & \text{else.} \end{cases} \quad (14a)$$

Similarly, the Y -direction gradient matrix is defined as

$$\text{Grad}_y(i, j) = \begin{cases} \frac{Z'_{x_0 y_0}(2, j) - Z'_{x_0 y_0}(1, j)}{d}, & i = 1, \\ \frac{Z'_{x_0 y_0}(m, j) - Z'_{x_0 y_0}(m-1, j)}{d}, & i = m, \\ \frac{Z'_{x_0 y_0}(i+1, j) - Z'_{x_0 y_0}(i-1, j)}{2d}, & \text{else.} \end{cases} \quad (14b)$$

Step 2. Sample out specific points in the two matrixes. In Grad_x , find out the points with the large gradient value (let us say for (i, j)), and according to (14a), add $(i, j+1)$ and $(i, j-1)$ to the point set U_1 . Similarly, in Grad_y , according to (14b), add $(i+1, j)$ and $(i-1, j)$ to the point set U_2 . Finally, take the element union of two sets.

$$U = U_1 \cup U_2, \quad (15)$$

where U is the final set of points for matching.

Step 3. Match. The MAD is rewritten as

$$D_{xy} = \frac{1}{\text{size}(U)} \sum_{(i,j) \in U} \left| Z_{xy}(i, j) - Z'_{x_0 y_0}(i, j) \right|, \quad (16)$$

where $\text{size}(U)$ represents the number of elements in the set U .

In this way, the improved TERCOM algorithm is constructed by replacing (6) with steps 1–3.

3.3. Preconditions for Application. From the comparison between (13) and (14a) and (14b), D_1 or D_2 is proportional to the value of their own gradient matrix, only when $d' = 2d$, as shown in Figure 2. Due to that D_1 or D_2 calculated with the points in U is relatively large, the side lobe interference in the real-time position would be comparably smaller, which ultimately improves the reliability of the position estimation.

Therefore, the algorithm works under the preconditions that

- (1) The matching direction of the algorithm must be consistent with the direction of gradient calculation;

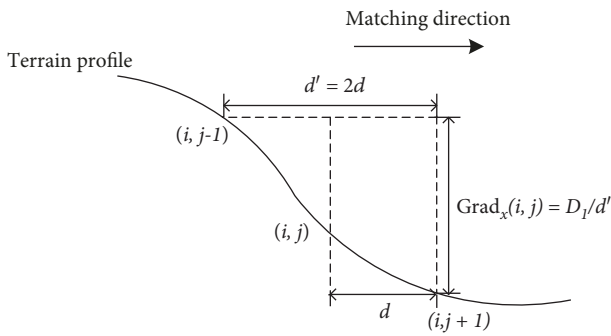


FIGURE 2: Illustration of the preconditions.

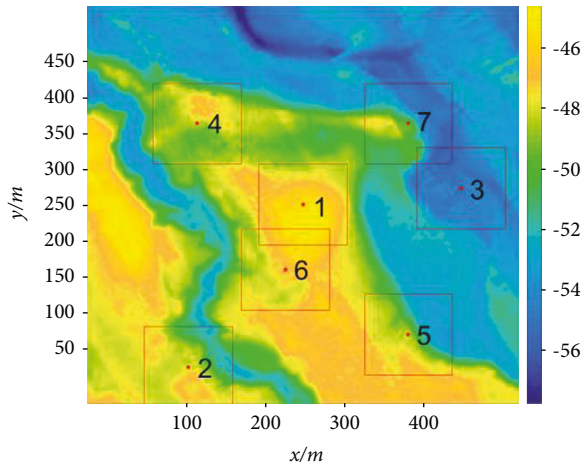


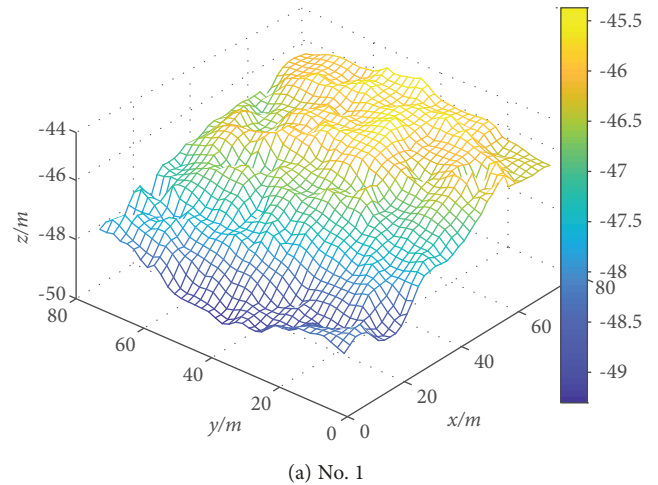
FIGURE 3: DEM and seven topographic regions.

that is, the horizontal matching direction corresponds to the X direction, and the vertical matching direction corresponds to the Y direction.

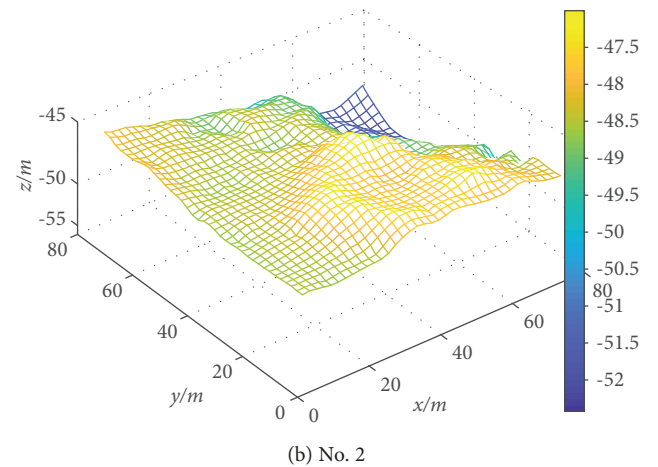
- (2) The intervals must be the same on matching and gradient calculation. It can be seen from (14a) and (14b) that $d' = 2d$. Certainly, the interval of the gradient calculation in (14a) and (14b) can be changed to satisfy the engineering precision demand.
- (3) The distribution of gradient values have been learnt, and according to the property of the fitting distribution, the corresponding point-sampling criteria have been set up, which makes the determination of the matching points more feasible and efficient.

3.4. Gradient Fitting Simulation. In order to determine the best distribution which fits the gradients of depth, the gradient data were compared with various standard distributions, i.e., normal, gamma, and Weibull. In the map, seven topographic regions are selected, numbered from 1 to 7, as shown in Figure 3.

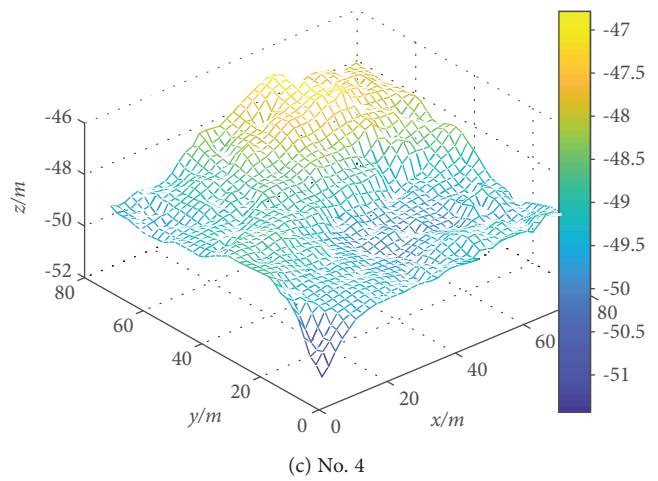
In fact, the mean of the gradient values is approximately zero, and the gradient values in the matrixes defined in (14a) and (14b) are symmetrically distributed at zero.



(a) No. 1



(b) No. 2

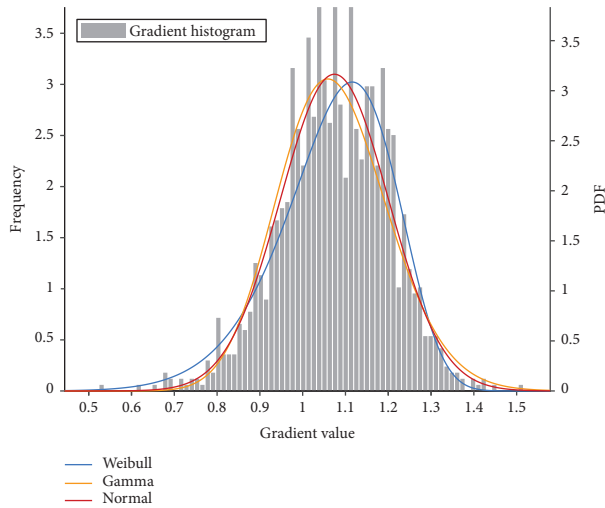


(c) No. 4

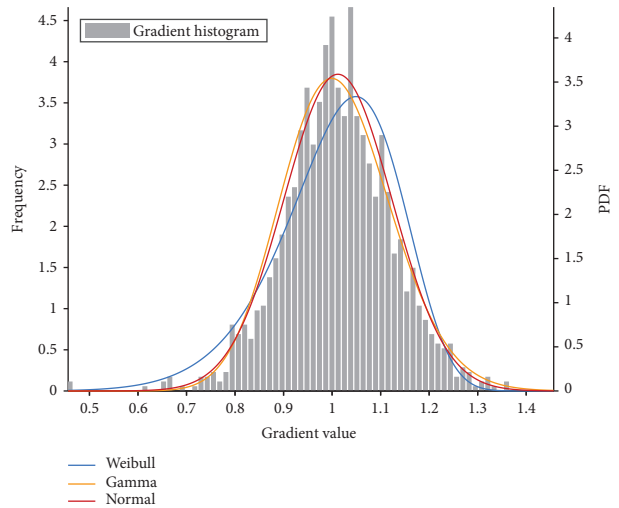
FIGURE 4: Landforms of three regions.

However, considering the properties of the gamma and Weibull distribution, a positive value is added to all the gradient values to ensure that they are distributed in the positive section.

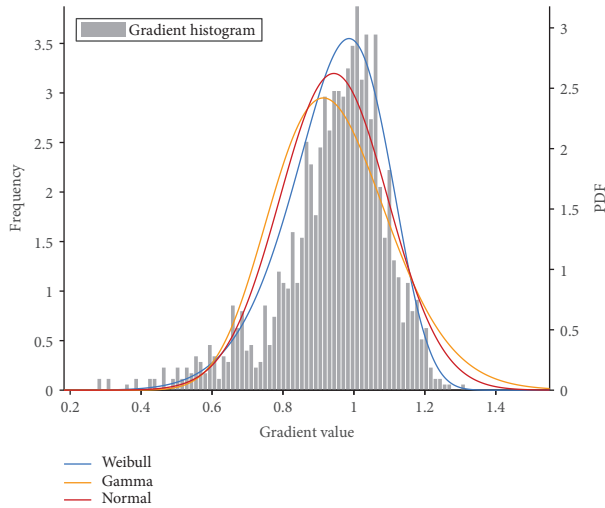
For the sake of clarity, taking region no. 1, no. 2, and no. 4 for example, their landforms are shown in Figures 4 and 5 which depict their frequencies of the gradient data in both X and Y direction as well as the PDF of normal, gamma,



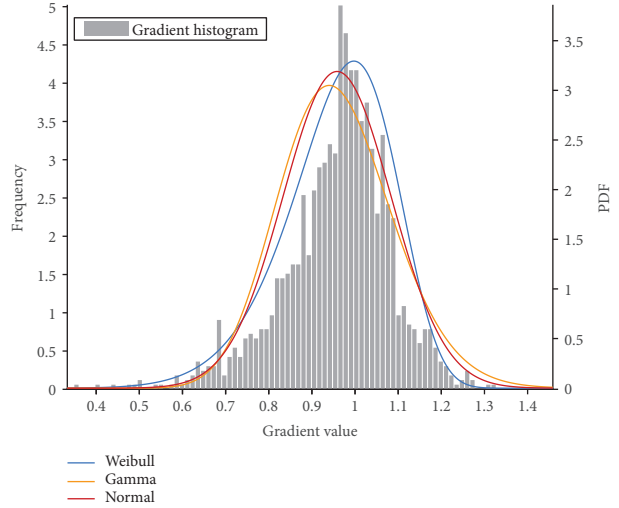
(a) No. 1 X direction fitting



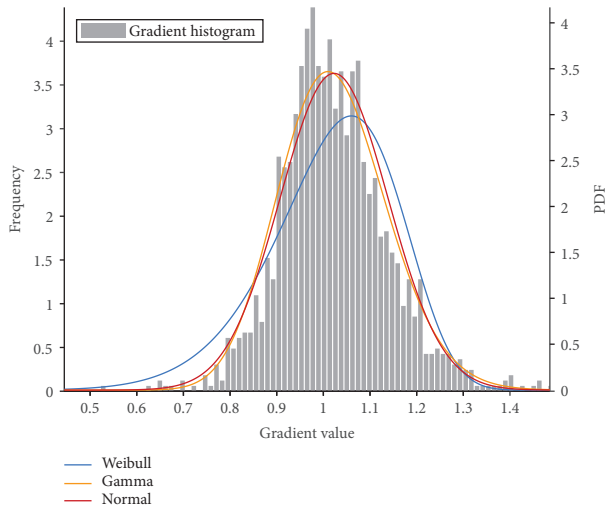
(b) No. 1 Y direction fitting



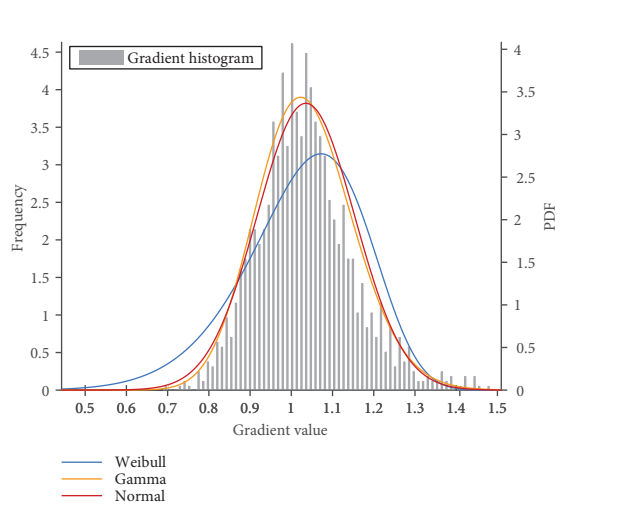
(c) No. 2 X direction fitting



(d) No. 2 Y direction fitting



(e) No. 4 X direction fitting



(f) No. 4 Y direction fitting

FIGURE 5: Results of gradient fitting.

TABLE 1: Parameters and MAE of X direction gradient fitting.

Region		1	2	3	4	5	6	7
Parameters	μ	1.0742	0.9434	0.9828	1.0229	0.8960	1.0427	0.8773
	σ	0.0874	0.1671	0.1010	0.1324	0.1886	0.1289	0.2354
	a	69.602	31.886	41.458	78.289	32.975	94.024	13.608
	b	64.796	33.800	42.185	76.535	36.802	90.178	15.512
	λ	1.1293	1.0034	1.0402	1.0752	0.9563	1.0901	0.9528
	k	9.4194	7.8748	8.0858	8.6665	7.1263	10.1016	5.4273
dk	Normal	0.2025	0.3192	0.3061	0.2108	0.3784	0.1589	0.3657
	Gamma	0.2253	0.3953	0.3702	0.1852	0.4458	0.1760	0.4407
	Weibull	0.2180	0.2214	0.2635	0.3691	0.3196	0.2533	0.3002

TABLE 2: Parameters and MAE of Y direction gradient fitting.

Region		1	2	3	4	5	6	7
Parameters	μ	1.0119	0.9583	0.9630	1.0353	0.9164	1.0185	0.9420
	σ	0.0773	0.1339	0.0950	0.1160	0.1457	0.1312	0.1643
	a	79.846	52.816	43.202	78.720	59.301	81.237	16.181
	b	78.904	55.114	44.861	76.036	64.714	79.759	17.177
	λ	1.0612	1.0105	1.0208	1.0895	0.9659	1.0690	1.0268
	k	9.5668	8.9917	7.6033	8.1490	8.9526	8.8259	5.0442
dk	Normal	0.1402	0.2812	0.2700	0.2261	0.3005	0.1550	0.2183
	Gamma	0.1529	0.3425	0.3243	0.1982	0.3566	0.1405	0.2740
	Weibull	0.2423	0.2199	0.2594	0.4166	0.2831	0.3053	0.1812

and Weibull distributions, which are given in (17), (18), and (19), respectively.

$$p_X(x; \mu, \sigma) = \frac{1}{\sqrt{2\pi}\sigma} \exp\left(-\frac{(x-\mu)^2}{2\sigma^2}\right), \quad (17)$$

$$p_X(x; a, b) = \begin{cases} \frac{b^a}{\Gamma(a)} x^{a-1} \exp(-bx), & x > 0, \\ 0, & x \leq 0, \end{cases} \quad (18)$$

$$p_X(x; \lambda, k) = \begin{cases} \frac{k}{\lambda} \left(\frac{x}{\lambda}\right)^{k-1} \exp\left(-\left(\frac{x}{\lambda}\right)^k\right), & x \geq 0, \\ 0, & x < 0, \end{cases} \quad (19)$$

where x is the value of the positive-transformed gradient, μ is the mean, σ is the standard deviation, b and λ are the scale parameters, a and k are shape parameters, and $\Gamma(a)$ is the gamma function. These parameters are calculated for each region and tabulated in Tables 1 and 2.

Then, to test how well the distribution resembles the gradient values, MAE between the frequencies and PDF values is calculated in (20).

$$dk = \frac{1}{M} \sum_{t=1}^M |h(t) - p(t)|, \quad (20)$$

where M is the total number of gradient histograms, t is the gradient level of each histogram, $h(t)$ is the frequency, and $p(t)$ is the probability density. The most fitting distribution has the lowest dk , and the results of the testing distributions are summarized in Tables 1 and 2.

3.5. Selection Criteria. As shown in the plots in Figure 5, three distribution curves are similar in shape and have a certain degree of fitting to the gradient values. As Figure 5(e) shows, when the number of negative gradients is more than the positive ones, the histogram is in a shape narrower on the left and wider on the right, and the gradients tend to obey the gamma distribution. In Figure 5(c), when the number of positive gradients is more than the negative ones, the shape of the histogram tends to be narrower on the right and wider on the left, and the gradients are inclined to obey the Weibull distribution. In Figure 5(b), when the number of positive and negative gradients is equal, the histogram is left-right symmetric, and the gradients fit the normal distribution best.

Although the result in Tables 1 and 2 reveals that Weibull distribution is generally smaller in dk , normal distribution appears to be more robust and universal for both positive and negative gradients. In addition, as is shown in Figures 6 and 7, 400 different regions are tested. The statistics in Table 3 shows that the dk of normal distribution has the smallest mean and variance.

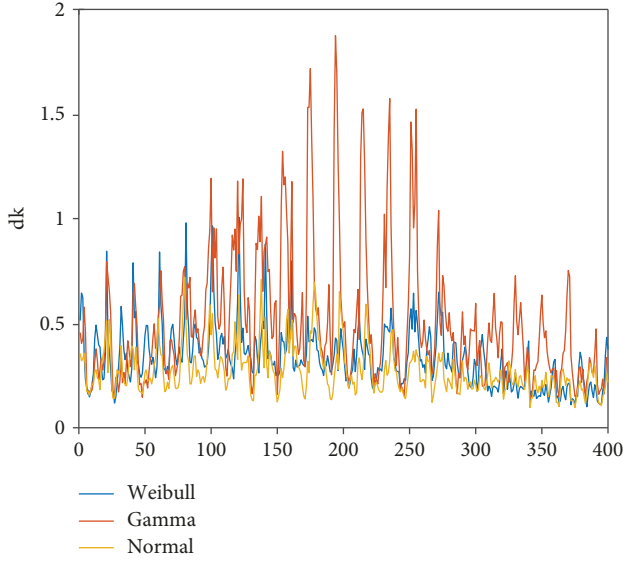


FIGURE 6: X-direction gradient fitting in 400 regions.

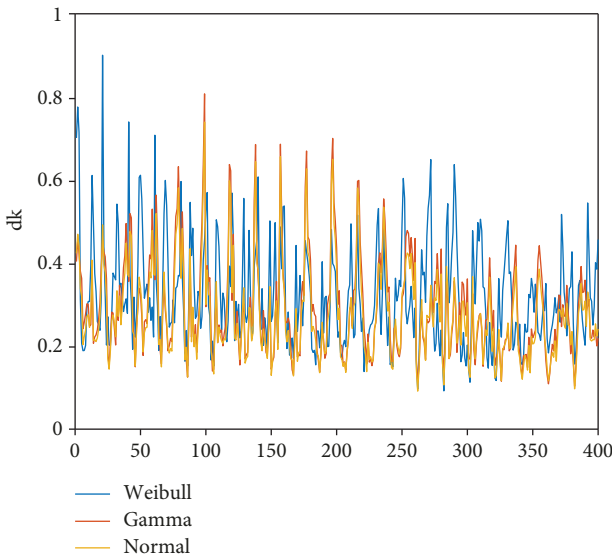


FIGURE 7: Y-direction gradient fitting in 400 regions.

TABLE 3: Statistics of dk in 400 regions.

		Normal	Gamma	Weibull
X direction	Mean	0.2758	0.2916	0.3202
	Variance	0.1085	0.1185	0.1248
Y direction	Mean	0.2712	0.5069	0.3313
	Variance	0.1099	0.3152	0.1443

Normal distribution is common in usage and simple in calculation as well. In conclusion, it is feasible to use normal distribution as the fitting curve of gradients and criteria of selecting matching points can be developed as follows.

First, estimate the normal distribution parameters.

$$\mu = \frac{1}{mn} \sum_{i=1}^m \sum_{j=1}^n \text{Grad}(i, j), \quad (21)$$

$$\sigma^2 = \frac{1}{mn} \sum_{i=1}^m \sum_{j=1}^n [\text{Grad}(i, j) - \mu]^2.$$

According to the 3-sigma rule, it can be approximately assumed that all gradients are distributed in interval $(\mu - 3\sigma, \mu + 3\sigma)$. The criterion can be given by

$$P(|\text{Grad}(i, j) - \mu| > \sigma) = 31.74\%. \quad (22)$$

Under this criterion, in both X and Y directions, 31.74% of the points with larger gradient values can be screened out as matching points through decision threshold σ . Finally, the set of matching points is determined in (15).

In many cases, a specific amount of matching points is required, and the criterion can be generalized as

$$P(|\text{Grad}(i, j) - \mu| > \Delta\sigma) = P_{\Delta}. \quad (23)$$

Therefore, the threshold $\Delta\sigma$ can be changed to approximately determine the amount of matching points.

4. Simulation

In this section, in order to evaluate the proposed algorithm, the estimation bias of three MAD-based TERCOM algorithms, respectively, matching with all points, uniform sampling points, and gradient-fitting sampling points, is firstly compared in different terrains, both flat and rough. Then, the influence of different thresholds in the generalized selection criterion on performance is studied in three different terrains. Finally, the optimal threshold of the selection criteria is given and the difference between the conventional algorithms and the improved algorithm in both error performance and computation is analyzed.

4.1. Localization Error Comparison. Assuming that 2025 of depth points are provided by the measurement in the matching region, the measured terrain elevation matrix in (2) with 45 rows and 45 columns can be built for matching. The purpose of MAD matching is to find the maximal $1/D$ from the matrix in (1) and determine the estimated position. The matching simulations of three sampling forms in a rough and flat terrain (shown in Figure 8) are shown in Figures 9 and 10, respectively.

In the rough terrain, Figure 9(a) shows the matching result of all 2025 points. The highest peak represents the estimated position as well as the true position. An interference position stands at the second-high peak, caused by the repetitive terrain. Figure 9(b) shows the matching result with 1444 points, uniformly sampled from measured data in the matching region. With the reduction in the amount of matching points, the peaks spread and the second-high peak becomes higher. While in Figure 9(c), matching with 1432 points sampled under the criterion defined in (22), the

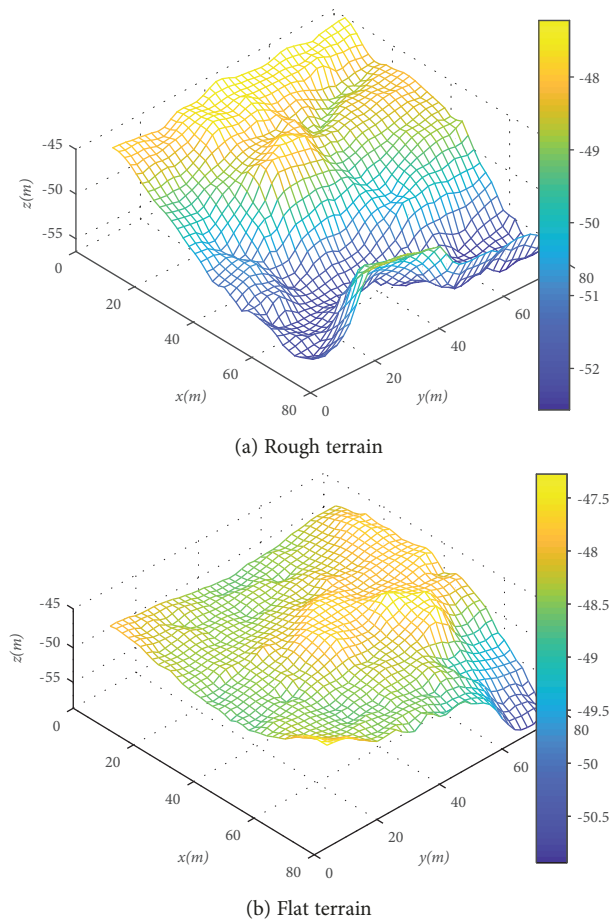


FIGURE 8: Two types of terrain for testing.

second-high peak collapses to a relatively low level and the uncertainty of the estimated position is narrowed. Figure 9(d) represents the matching result with 841 uniform sampling points. As shown in the figure, a new disturbance occurs as the price of the point reduction. Moreover, Figure 9(e) represents the matching result with 795 points sampled under the generalized criterion (23) with $\Delta = 1.5$. Even if the number of matching points is further reduced, the certainty of the true position is not lowered compared to Figure 9(a). Therefore, in the rough terrain, the matching method under the gradient fitting criteria can effectively reduce the influence of repetitive terrain.

In the flat terrain, however, the risk of a false position fix increases as there are more interferential peaks, which is mainly caused by the similarity of nearby regions. Figure 10(a) shows the matching result of all 2025 points. Compared with Figure 10(a), the highest peak also represents the estimated position as well as true position, whereas the number of interference positions increases. Figure 10(b) represents the matching result of 1444 uniform sampling points, and there is a serious expansion of the highest peak, which ultimately results in the bias of the position estimation, while Figure 10(c), representing the result of 1397 points sampled under the criterion defined in (22), shows the same certainty of the position estimation as Figure 10(a). As the number of

uniform sampling points further reduces to 841, Figure 10(d) shows a great deviation between estimated and true positions, while Figure 10(e) represents the matching result with 804 points sampled under the generalized criterion (23) with $\Delta = 1.5$. Even though its number of matching points is comparable to Figure 10(d) and far less than Figure 10(a), its certainty and accuracy of the estimated position are higher than Figure 10(d) and comparable to Figure 10(a). Therefore, in the flat terrain, the matching method under the gradient fitting criteria can effectively reduce the influence of the adjacent terrain.

4.2. Optimum Threshold and Computation Complexity. The robustness of TERCOM based on gradient fitting is already confirmed in Section 4.1, and the performance of this method varies with Δ in (23), which determines the number of matching points and so is the computation. It is noteworthy that $\Delta = 0$ represents the matching with all points, and with the increase in Δ , the matching points decrease together with its compute. In this section, the localization performance under different Δ is studied by Monte-Carlo simulation, which can be written as

$$e = \frac{1}{L} \sum_{l=1}^L \sqrt{(\hat{x}_{0l} - x_0)^2 + (\hat{y}_{0l} - y_0)^2}, \quad (24)$$

where L represents the simulation times, (x_0, y_0) is the true position, $(\hat{x}_{0l}, \hat{y}_{0l})$ is the estimated position for the l th experiment, and the result e is evaluated as matching error, indicating the mean deviation of the position estimation. The curves in Figure 11 reveal the movement of e with increasing Δ in three different terrains ($L = 5000$).

All of the curves in Figure 11 present the same tendency of the matching error, monotonically decreasing in $(0, 1)$, reaching the minimum at $\Delta = 1$, which is called min level, and monotonically increasing in $(1, 3)$. Moreover, when $\Delta \in (1.2, 1.4)$, the error approximately reaches the level at $\Delta = 0$, which is called all-point level. Although the number of matching points decreases as Δ increases, the matching error would become huge when $\Delta = 2$ or larger. Therefore, endlessly increasing Δ to reduce computational complexity is not feasible.

However, due to the low fluctuation of terrain no. 3, the matching errors are generally large, and there would be a vast horizontal disparity between all-point level and min level, as shown in Figure 11(a). In Figure 11(b), terrain no. 5 has a higher degree of fluctuation, and the matching error is generally small, so the difference between the two levels is smaller. The performance in the moderate undulating terrain no. 6 is sort of in between, as shown in Figure 11(c).

In summary, the limitation of error reduction varies by terrain, but the choices of Δ remain to be consistent. For the balance between matching error and computation complexity, the optimum choice of Δ should be within $(1, 1.2)$, where the amount of matching points is relatively small, and the matching error is also close to the theoretical minimum. In this way, it can be approximated that (22) is the best criterion with optimum threshold. Under this

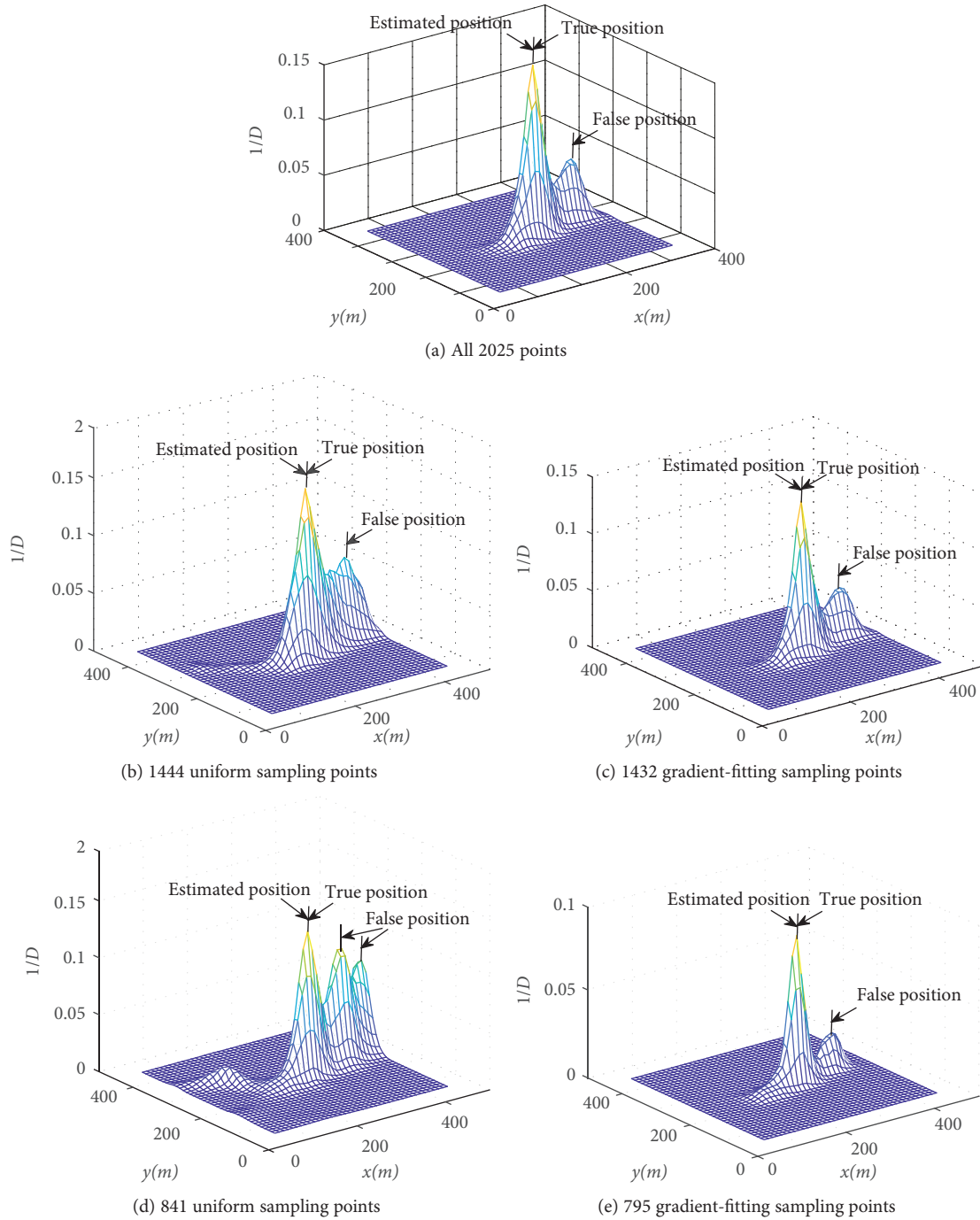


FIGURE 9: Matching performance with different matching points in rough terrain.

criterion, the matching performance of the proposed gradient-fitting method is compared with the two conventional methods mentioned above. The results are listed in Table 4.

In Table 4, σ_x and σ_y represent the standard deviations of the gradient in the X and Y directions, respectively, so as to determine the degree of terrain fluctuation. The result in the table shows that the higher fluctuation of the terrain is that, the lower the matching error becomes, the smaller the difference is between the three. However, the proposed matching algorithm has less matching error than the two

conventional algorithms, regardless of the degree of fluctuation. Furthermore, compared with the all-point matching method, the proposed algorithm filters out an average of 609 points and retains an average of 1416 points for matching to achieve a larger error reduction. It explains that the filtered points have a certain interference to the position estimation and the remaining points are enough to characterize the topographic information, which radically reduces the estimation error as well as the compute. This also verifies the previous theoretical analysis and superiority of the proposed algorithm.

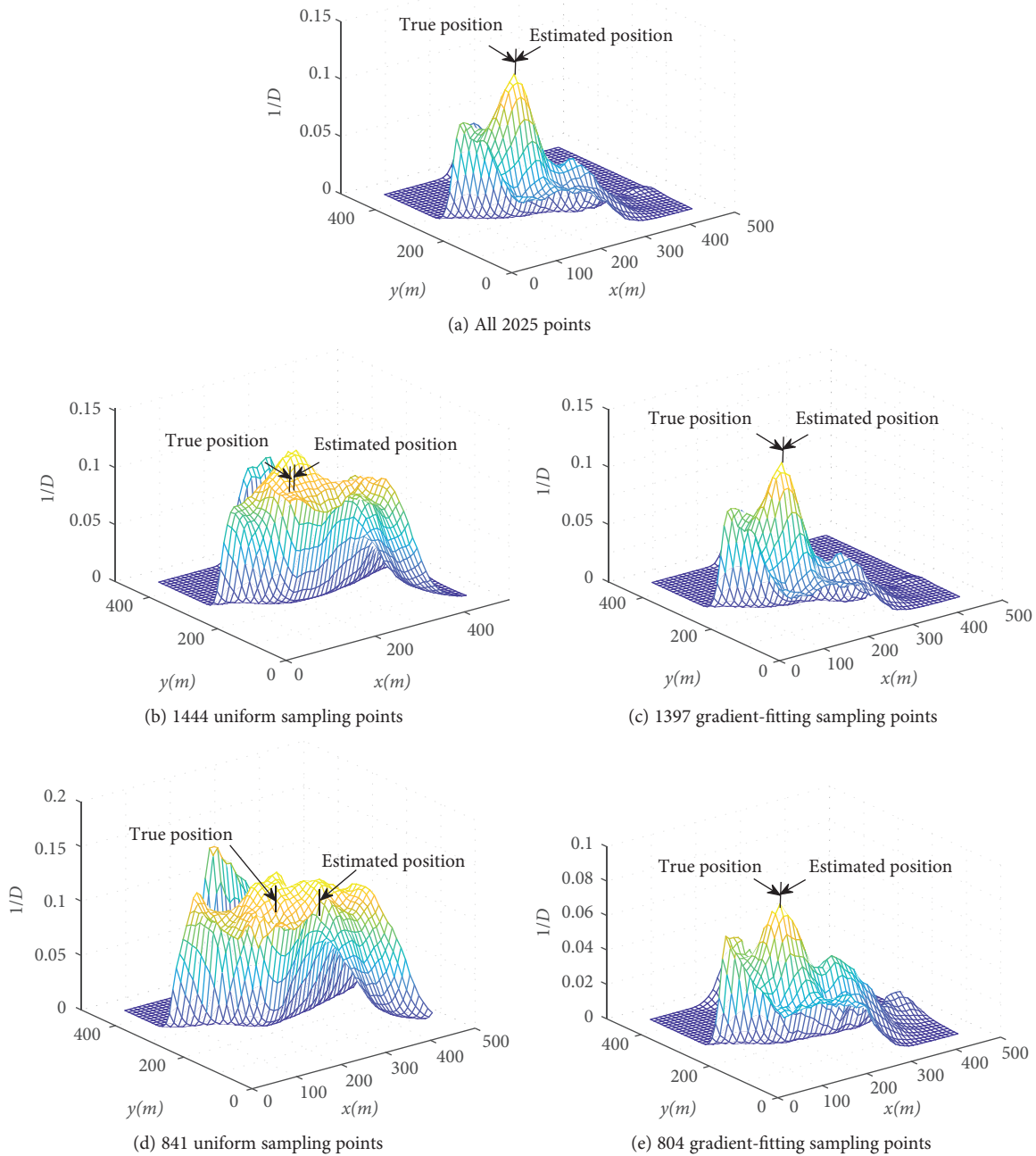


FIGURE 10: Matching performance with different matching points in a flat terrain.

In terms of the compute, the complexity of the proposed algorithm is mainly determined by the amount of matching points J and the number of reference positions K . The amount of computation can be approximated as $J \times K$, that is, proportional to J with a proportionality coefficient K . Therefore, the change in computational complexity can be evaluated by the change of points with Δ , which is shown in Figure 12.

The best Δ is within (1,1.2), and the matching error is closest to minimum when $\Delta = 1$. As is shown in Figure 9, when $\Delta = 1$, the compute is reduced by $(2025 - 1416) \times K = 609K$, and when $\Delta = 1.2$, the computation is reduced

by $(2025 - 1150) \times K = 875K$. More importantly, in actual matching, K would be larger, thus the reduction of the compute would be more significant.

5. Conclusion and Future Work

In this paper, an improved matching algorithm is proposed to overcome the shortcomings of the conventional matching algorithm. The simulation results show that the improved algorithm not only has better matching performance but also greatly reduces the computational cost. Meanwhile, the applicability of the normal distribution in gradient

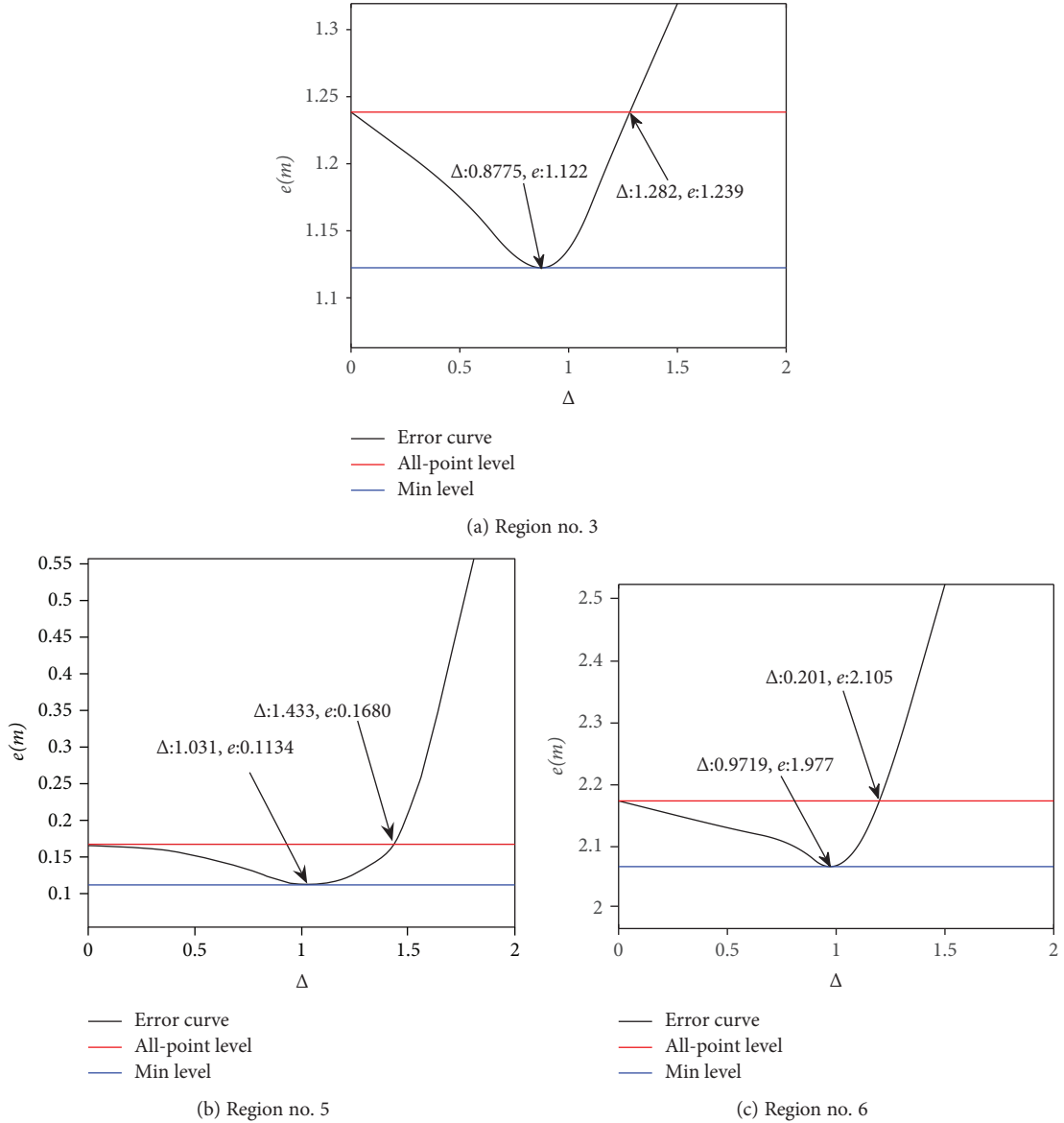


FIGURE 11: Error curves of three terrains.

TABLE 4: Matching error comparison of three methods.

	Region	1	2	3	4	5	6	7
Fluctuation	σ_x	0.0874	0.1671	0.1010	0.1324	0.1886	0.1289	0.2354
	σ_y	0.0773	0.1339	0.0950	0.1160	0.1457	0.1312	0.1643
Number of matching points	All	2025	2025	2025	2025	2025	2025	2025
	Uniform	1444	1444	1521	1444	1444	1521	1444
	Grad-fit	1385	1435	1450	1376	1389	1452	1428
e (m)	All	2.8293	0.6474	1.2387	1.2078	0.1680	2.1053	0.2680
	Uniform	6.4865	2.0072	3.5304	2.2676	0.3186	6.8306	0.5573
	Grad-fit	2.6418	0.5448	1.1272	1.0042	0.1106	1.9543	0.2153

fitting is verified, corresponding criteria for sampling are given, and the algorithm gains the smallest localization error under the criterion with $\Delta = 1$. Under this sampling

criterion, the improved algorithm can better account for “computation” and “accuracy” to improve the matching positioning performance.

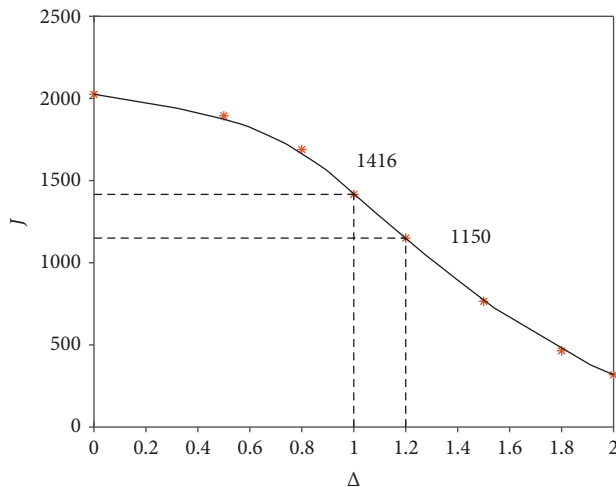


FIGURE 12: The regulation of point reduction.

In fact, the proposed method can be a step in the current trend of navigation like using Bayesian methods to process dense terrain sensor measurements. Real-time positioning is hardly questionable with today's computational power as well as the reduction in matching points. Also, compared to the conventional matching method, the proposed method gains higher positioning accuracy due to its unique sampling criterion. However, in our current study, there is no single evidence yet to prove the applicability and validity of the algorithm in mainstream navigation methods. Therefore, we will improve this part in our future work.

Data Availability

The terrain depth data used to support the findings of this study are available from the corresponding author upon request. All other data are shown above in the form of tables or charts.

Conflicts of Interest

The authors declare that they have no conflicts of interest.

Acknowledgments

This research was sponsored by the National Natural Science Foundation of China under Grants U1709203 and 41376103 and Research Foundation of Qingpu District 2018-14 (corresponding author: Tian Zhou) The authors are with the Underwater Acoustic Science and Technology Laboratory, College of Underwater Acoustic Engineering, Harbin Engineering University, Harbin, China (e-mail: zhoutian@hrbeu.edu.cn).

References

- [1] H. Zhao and Z. Y. Wang, "Motion measurement using inertial sensors, ultrasonic sensors, and magnetometers with extended Kalman filter for data fusion," *IEEE Sensors Journal*, vol. 12, no. 5, pp. 943–953, 2012.
- [2] W. Budiman, M. Shanmugavel, V. Ragavan, and S. B. Lazarus, "A low-cost underwater navigation system for remotely operated underwater vehicle — design, system-integration, and implementation," in *2014 IEEE International Conference on Computational Intelligence and Computing Research*, pp. 1–4, Coimbatore, India, December 2014.
- [3] L. Paull, S. Saeedi, M. Seto, and H. Li, "AUV navigation and localization: a review," *IEEE Journal of Oceanic Engineering*, vol. 39, no. 1, pp. 131–149, 2014.
- [4] M. A. Green, "Recollections of superconductivity work at LBL and KfK from 1965 through the 1980s," *IEEE Transactions on Applied Superconductivity*, vol. 27, no. 4, pp. 1–8, 2017.
- [5] R. Costanzi, N. Monnini, A. Ridolfi, B. Allotta, and A. Caiti, "On field experience on underwater acoustic localization through USBL modems," in *OCEANS 2017*, pp. 1–5, Aberdeen, UK, June 2017.
- [6] Ø. Hegrenæs, A. Ramstad, T. Pedersen, and D. Velasco, "Validation of a new generation DVL for underwater vehicle navigation," in *2016 IEEE/OES Autonomous Underwater Vehicles (AUV)*, pp. 342–348, Tokyo, Japan, November 2016.
- [7] H. P. Yu, Y. L. Geng, H. Zhu, N. Jiang, and J. H. Chen, "A novel filtering model for DVL aided inertial navigation system based on observability degree analysis," in *2016 IEEE Chinese Guidance, Navigation and Control Conference (CGNCC)*, pp. 94–97, Nanjing, China, August 2016.
- [8] A. Howard and H. Seraji, "An intelligent terrain-based navigation system for planetary rovers," *IEEE Robotics & Automation Magazine*, vol. 8, no. 4, pp. 9–17, 2001.
- [9] M. Lager, E. A. Topp, and J. Malec, "Underwater terrain navigation using standard sea charts and magnetic field maps," in *2017 IEEE International Conference on Multisensor Fusion and Integration for Intelligent Systems (MFI)*, pp. 78–84, Daegu, South Korea, November 2017.
- [10] Y. R. Han, B. Wang, Z. H. Deng, S. T. Wang, and M. Y. Fu, "A mismatch diagnostic method for TERCOM-based underwater gravity-aided navigation," *IEEE Sensors Journal*, vol. 17, no. 9, pp. 2880–2888, 2017.
- [11] J. H. Zhao, K. Zhang, H. M. Zhang, and K. Yang, "Study on underwater terrain matching positioning based on the integration of TERCOM and MCTM," in *OCEANS'10 IEEE SYDNEY*, pp. 1–4, Australia, May 2010.
- [12] G. N. Yuan, H. W. Zhang, K. F. Yuan, and L. Zhu, "Improved SITAN algorithm in the application of aided inertial navigation," in *Proceedings of 2012 International Conference on Measurement, Information and Control*, pp. 922–926, Harbin, China, May 2012.
- [13] M. Li, Y. Liu, and L. P. Xiao, "Performance of the ICCP algorithm for underwater navigation," in *2014 International Conference on Mechatronics and Control (ICMC)*, pp. 361–364, Jinzhou, China, July 2014.
- [14] H. M. J. Cantalloube, "High altitude terrain correlation navigation resetting by nadir looking synthetic aperture radar," in *2017 Progress In Electromagnetics Research Symposium - Spring (PIERS)*, pp. 3252–3257, St Petersburg, Russia, May 2017.
- [15] D. D. Peng, T. Zhou, H. S. Li, and W. Y. Zhang, "Terrain aided navigation for underwater vehicles using maximum likelihood method," in *2016 IEEE/OES China Ocean Acoustics (COA)*, pp. 1–6, Harbin, China, January 2016.
- [16] N. Fairfield and D. Wettergreen, "Active localization on the ocean floor with multibeam sonar," in *OCEANS 2008*, pp. 1–10, Quebec, Canada, September 2008.

- [17] K. B. Énonsen and O. K. Hagen, "Recent developments in the HUGIN AUV terrain navigation system," in *OCEANS'11 MTS/IEEE KONA*, pp. 1–7, Waikoloa, HI, USA, September 2011.
- [18] D. K. Meduna, S. M. Rock, and R. S. McEwen, "Closed-loop terrain relative navigation for AUVs with non-inertial grade navigation sensors," in *2010 IEEE/OES Autonomous Underwater Vehicles*, pp. 1–8, Monterey, CA, USA, September 2010.
- [19] K. Zhang, H. M. Zhang, C. Shi, and J. H. Zhao, "Underwater navigation based on topographic contour image matching," in *2010 International Conference on Electrical and Control Engineering*, pp. 2494–2497, Wuhan, China, June 2010.
- [20] J. Shen, J. Y. Zhang, and X. Luo, "The application of image edge detection in matching region selection of underwater terrain-aided navigation," in *2010 International Conference on Computational Intelligence and Software Engineering*, pp. 1–4, Wuhan, China, December 2010.
- [21] S. I. Adzhani, H. Mahmudah, and T. B. Santoso, "Time-frequency analysis of underwater ambient noise of mangrove estuary," in *2016 International Electronics Symposium (IES)*, pp. 223–227, Denpasar, Indonesia, September 2016.
- [22] M. V. Jamali, P. Khorramshahi, A. Tashakori et al., "Statistical distribution of intensity fluctuations for underwater wireless optical channels in the presence of air bubbles," in *2016 Iran Workshop on Communication and Information Theory (IWCIT)*, pp. 1–6, Tehran, Iran, May 2016.
- [23] C. Kurnaz and B. K. Engiz, "Distribution fitting for long term electric field strength measurements," in *2017 40th International Conference on Telecommunications and Signal Processing (TSP)*, pp. 267–270, Barcelona, Spain, July 2017.



Hindawi

Submit your manuscripts at
www.hindawi.com

